



**HAL**  
open science

## Enhanced volatile organic compound sensing properties of BiFeO<sub>3</sub> by carbon fibres addition

Bertrand Boudart, Yannick Guhel, Nouara Lamrani-Amaouz, Rachida Douani, Ahcene Chaouchi, M'hand Oughanem

► **To cite this version:**

Bertrand Boudart, Yannick Guhel, Nouara Lamrani-Amaouz, Rachida Douani, Ahcene Chaouchi, et al.. Enhanced volatile organic compound sensing properties of BiFeO<sub>3</sub> by carbon fibres addition. Processing and Application of Ceramics, 2022. hal-03900490

**HAL Id: hal-03900490**

**<https://hal.science/hal-03900490v1>**

Submitted on 15 Dec 2022

**HAL** is a multi-disciplinary open access archive for the deposit and dissemination of scientific research documents, whether they are published or not. The documents may come from teaching and research institutions in France or abroad, or from public or private research centers.

L'archive ouverte pluridisciplinaire **HAL**, est destinée au dépôt et à la diffusion de documents scientifiques de niveau recherche, publiés ou non, émanant des établissements d'enseignement et de recherche français ou étrangers, des laboratoires publics ou privés.



## Enhanced volatile organic compound sensing properties of BiFeO<sub>3</sub> by carbon fibres addition

M'hand Oughanem<sup>1,\*</sup>, Rachida Douani<sup>1</sup>, Nouara Lamrani<sup>1</sup>, Yannick Guhel<sup>2</sup>, Ahcène Chaouchi<sup>1</sup>, Bertrand Boudart<sup>2</sup>

<sup>1</sup>Laboratoire de Chimie Appliquée et Génie Chimique, Univ. UMMTO, Tizi Ouzou, Algérie

<sup>2</sup>Université de Caen Normandie, ENSICAEN, CNRS, GREYC, 14000 Caen, France

Received 30 March 2022; Received in revised form 29 June 2022; Accepted 13 September 2022

### Abstract

*In the present work, pure BiFeO<sub>3</sub> (BFO) particles were synthesized by sol-gel method and mixed with carbon fibre to form composites (x%CFs-BFO, where x corresponds to 0, 4, 8 and 10 wt.%) by hydrothermal treatment at 150 °C. The resulting composite powders were characterized by X-ray diffraction, Raman spectroscopy, nitrogen adsorption/desorption isotherm and scanning electron microscopy (SEM-EDX). The synthesized powders were used for gas sensors preparation by manual deposition of their mixture with polyvinyl alcohol on alumina tubes ending with two silver electrodes. The impedance of the sensitive layers was determined by impedance spectroscopy in the temperature range 100–250 °C at different gaseous concentrations. The detection properties of the fabricated sensors for various volatile organic compounds were investigated. The sensors showed better sensitivity to acetone compared to other gases. The addition of carbon fibres improved the sensitivity to acetone vapour from 64 to 135% at 100 ppm and reduced the optimum operating temperature of the sensors by 20 °C and the response and recovery times from (26 s/15 s) to (18 s/10 s). This study revealed that x%CFs-BiFeO<sub>3</sub> composites are promising candidates for gas sensors.*

**Keywords:** BiFeO<sub>3</sub>, carbon fibres, composite, gas sensor, sensitivity

### I. Introduction

Volatile organic compounds (VOCs) are large families of substances that can easily evaporate under normal conditions. They are mainly composed of hydrocarbons and various organic compounds. The extreme volatility of these compounds can lead to various direct and indirect health effects [1]. The direct effects are mainly due to inhalation; VOCs can cause skin and respiratory irritations, headaches, heart, digestive and kidney disorders, concentration or memory problems [2]. Some VOCs are also known to have carcinogenic properties (benzene, formaldehyde) [3]. Acetone is a very common VOC used in various laboratory works and in the chemical and pharmaceutical industries. It is a colourless, reactive and highly volatile compound, which is very harmful in its gaseous form [4]. Constant inhalation of acetone can cause severe headaches and when its concentration exceeds 173 ppm, it can cause irrita-

tion of the respiratory system and narcosis which can severely damage the nervous system [5]. Moreover, it is flammable with lower explosive limit (LEL) and upper explosive limit (UEL) of 2.6 and 12.8%, respectively [6]. Consequently, acetone concentrations in industrial and laboratory environments need to be monitored for environmental and health safety purposes.

Metal oxides are considered the most promising materials for the design of gas sensing layers [7]. Due to their properties, such as high gas sensitivity and good selectivity, they are usually the most suitable candidates for the development of sensitive layers [8]. Among the various metal oxides, perovskite BiFeO<sub>3</sub>, which is a multifunctional p-type semiconductor, has good sensing properties [9] in addition to its good multiferroic properties at room temperature [10]. Moreover, it has been commonly used as a gas and humidity sensors for: LPG gas [11], ammonia [12], SO<sub>2</sub> [13], ethanol [14,15], acetone [16,17], humidity [18] and other applications, such as photocatalysts [19,20], solar cells [21,22], etc.

Due to their various physical and chemical proper-

\*Corresponding author: tel: +213 668 462 387  
e-mail: [mhand.oughanem@ummto.dz](mailto:mhand.oughanem@ummto.dz)

ties, carbon compounds in their different morphological forms such as fibre [23], nanotube (CNT) [24], and graphene [25], have been widely studied for their potential application in sensors as materials for reinforcing and improving the detection properties of sensitive layers based on semiconductor oxides [26–28]. For instance, Kaur *et al.* [29] reported that the addition of reduced graphene oxide (rGO) to Gd-doped  $\text{WO}_3$  led to a significant increase in acetone response with a reduction in the optimum operating temperature and improved selectivity. According to the authors, the improved gas sensing performance of the Gd- $\text{WO}_3$ /rGO nanostructures can be attributed to the formation of heterojunctions between the p-type rGO and the n-type  $\text{WO}_3$ , the large specific surface area of the composite and the high electron conductivity of the rGO [29]. Mendoza *et al.* [30] demonstrated that  $\text{SnO}_2$ -CNTs sensors have a better sensitivity to hydrogen sulphide and alcohol vapours than pure  $\text{SnO}_2$ . On the other hand, Zhang *et al.* [31] noted that the sensitivity of the layer based on the rGO- $\text{Fe}_2\text{O}_3$  composite increases with increasing rGO levels in the composite. In another study [32], they reported an improvement in sensitivity and response time with a decrease in sensor operating temperature from 125 °C for  $\alpha$ - $\text{Fe}_2\text{O}_3$  to room temperature for the 12.2% G/ $\alpha$ - $\text{Fe}_2\text{O}_3$  composite. Hojati *et al.* [33] pointed out that hydrothermally synthesized ZnO/MWCNT nanosheets exhibited stronger CO sensing characteristics than pure ZnO.

The objective of this study is the enhancement of the VOCs detection properties of sensors based on the perovskite BFO structure by using carbon fibres as additives. The influence of the incorporation of carbon fibres (CFs) on the structural and morphological characteristics of the resulting layer (CFs-BFO) has also been studied.

## II. Experimental

### 2.1. Preparation of CFs-BiFeO<sub>3</sub> composites

In this work, the chemical reagents of high analytical purity were used: ferric nitrate(III) nonahydrate ( $\text{Fe}(\text{NO}_3)_3 \cdot 9 \text{H}_2\text{O}$ , 99%), bismuth nitrate pentahydrate ( $\text{Bi}(\text{NO}_3)_3 \cdot 5 \text{H}_2\text{O}$ , 99%), nitric acid ( $\text{HNO}_3$ , 69%), citric acid monohydrate ( $\text{C}_6\text{H}_8\text{O}_7 \cdot \text{H}_2\text{O}$ , 99.5%), carbon fibres and deionized water.

Firstly, the BFO particles were prepared through the typical sol-gel method where 2.5468 g of  $\text{Bi}(\text{NO}_3)_3 \cdot 5 \text{H}_2\text{O}$  and 2.02 g of  $\text{Fe}(\text{NO}_3)_3 \cdot 9 \text{H}_2\text{O}$  were initially dissolved into 10 ml  $\text{HNO}_3$  (Fig. 1). Subsequently, 5.0708 g of citric acid in 50 ml deionized water as a complexing agent were added into the mixture and stirred at 80 °C until gel was formed. The obtained gel was dried at 120 °C, calcined at 350 °C for 2 h in air and finally at 700 °C for 2 h at a rate of 5 °C/min.

In the next step, the CFs-BiFeO<sub>3</sub> composites were synthesized from carbon fibres and BFO powder via a simple hydrothermal process (Fig. 1b). Different amount of CFs were dispersed in 25 ml of  $\text{H}_2\text{O}$ . The obtained solutions were added to aqueous suspensions of BFO (10 mg/ml) under ultrasound. Then, the resulting mixtures were transferred to autoclaves and heated at 150 °C for 6h, and then cooled to room temperature. Finally, the as-prepared CFs-BFO composites were washed with deionized water and dried at 100 °C before further use. The samples containing 0, 4, 8 and 10 wt.% CFs are noted BFO, 4%CFs-BFO, 8%CFs-BFO and 10%CFs-BFO, respectively.

### 2.2. Material characterization

Thermogravimetric analysis (TGA) and differential thermal analysis (DTA) were carried out using a thermal

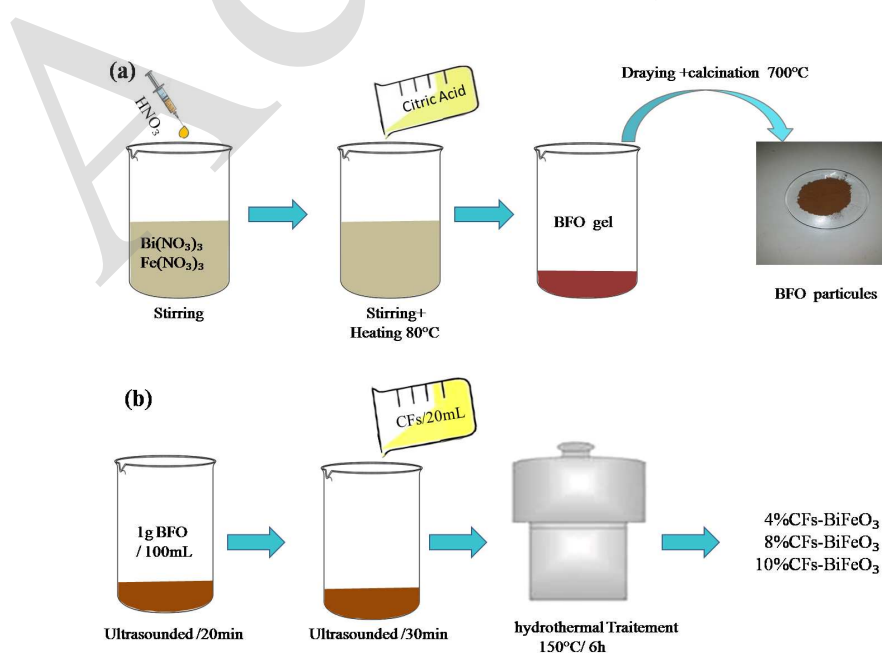


Figure 1. Different steps of the synthesis: a) synthesis of BiFeO<sub>3</sub> particles; b) synthesis of composite CFs-BFO

analyser type LABSYS<sub>Sevo</sub>. Surface morphology of the prepared BFO and CFs-BFO composite powders were examined with a JEOL SEM7200 microscope equipped with an EDX system (BRUKER system). The samples were prepared by dispersion of the powder in alcohol, under ultrasound, then a drop of the mixture was deposited on a carbon membrane supported by a TEM grid (Cu) followed by a fast metallization in a gold evaporator, to avoid charge effects. Crystallographic structure and the effect of carbon fibre addition on crystallinity of the BFO nanoparticles were investigated using X-ray diffraction (diffractometer type Panalytical Empyrean DRX with Cu K $\alpha$  (1.5406 Å) radiation at 45 kV). The synthesized particles were also characterized by using Raman spectroscopy (InVia spectrometer from Renishaw using a visible laser with a wavelength of 632.8 nm). BET specific surface area of the materials was determined by measuring the nitrogen adsorption-desorption contents. The measurements were carried out by utilizing Quantachrome instrument driven by Nova Win software. Impedance measurements of the samples were carried out by LCR HP 2484A meter at a frequency of 1 kHz and a bias of 1 V.

### 2.3. Sensors preparation and sensing measurements

Precursor pastes, obtained by mixing of the synthesized powders with polyvinyl alcohol, were manually deposited on the alumina tubes ending with two silver electrodes. Two silver wires were connected with the silver electrodes to make contact leads. After that, the sensors were initially aged at 300 °C for 24 h in air to achieve the desired stability before measurements. Gas detection measurements were performed using a homemade gas test chamber (51 in volume) integrated with LCR meter to measure electrical impedance changes in the presence and absence of target gas molecules. The desired concentrations of the testing gases were obtained by the static liquid gas distribution method, and calculated by the following formula [34]:

$$C = \frac{22.4 \rho \cdot \sigma \cdot V_1}{M \cdot V_2} \quad (1)$$

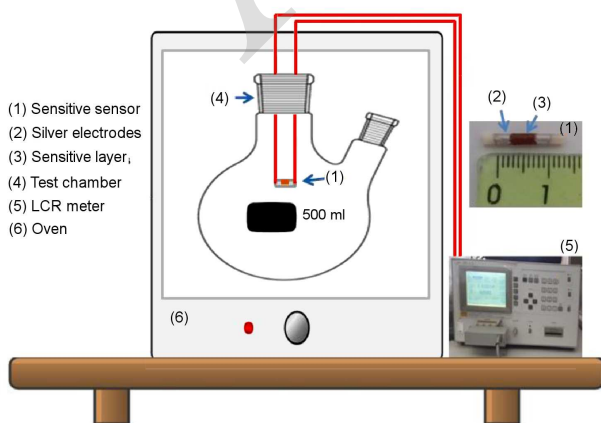


Figure 2. Schematic of the measuring device

where  $C$  (ppm) is the required concentration of the test gas,  $\rho$  (g/ml) is the density of the corresponding liquid,  $\sigma$  is the desired gas volume fraction,  $V_1$  ( $\mu$ l) is the volume of the liquid,  $M$  (g/mol) is the molecular weight of the liquid and  $V_2$  (l) is the volume of the test chamber.

Once the liquid volume was fixed, the sensor was placed in the closed test chamber. Then the assembly was transferred to an oven to keep the sensor working at a high temperature. An illustrative schematic of the measuring device is shown in Fig. 2.

## III. Results and discussion

### 3.1. Morphological and structural characterizations

Calcination temperature of the BFO samples was estimated by thermogravimetric analysis (TGA/DTA). Figure 3 shows two stages of thermal decomposition. In the first one, a very weak endothermic effect appears around 200 °C and corresponds to the evaporation of adsorbed water molecules. In the second one, a drastic weight loss (62.29%) occurs between 200 and 500 °C. This loss can be explained by the combustion of the organic precursors and non-carbonized NO<sub>3</sub><sup>-</sup> anions which is confirmed by the rapid and intense exothermic peak at 307 °C [35]. In contrast, no mass loss was observed between 500 and 800 °C. Consequently, we opted for a calcination temperature of 700 °C.

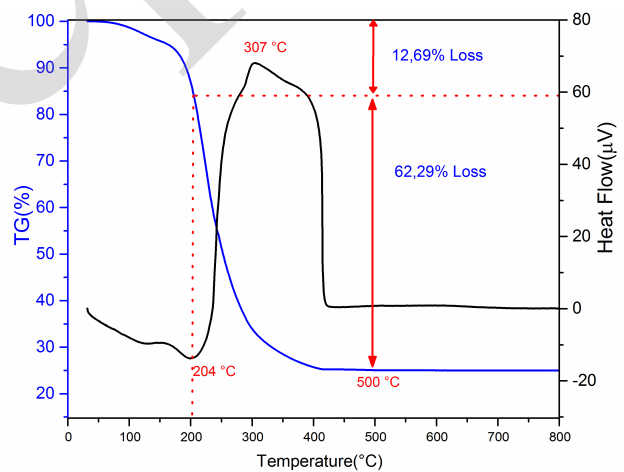


Figure 3. TGA/DTA analysis of the uncalcined BiFeO<sub>3</sub> powder

The morphologies and compositions of the as-prepared BiFeO<sub>3</sub> and CFs-BiFeO<sub>3</sub> samples were studied by SEM/EDX. The SEM images (Fig. 4) show the presence of crystals with irregular shape and others that appear as platelets which obviously have 2D growth tendency. They also reveal a heterogeneous distribution of grain size. EDX analysis confirmed that the pure BFO sample contains main three elements, Bi, Fe and O, as well as traces of Ca, Mg and Al whose levels are lower than 1%. The results presented in Table 1 give the average values over a set of grains (spectra) having approximately the same composition for each powder. The results are rather uniform and consistent with the BiFeO<sub>3</sub>

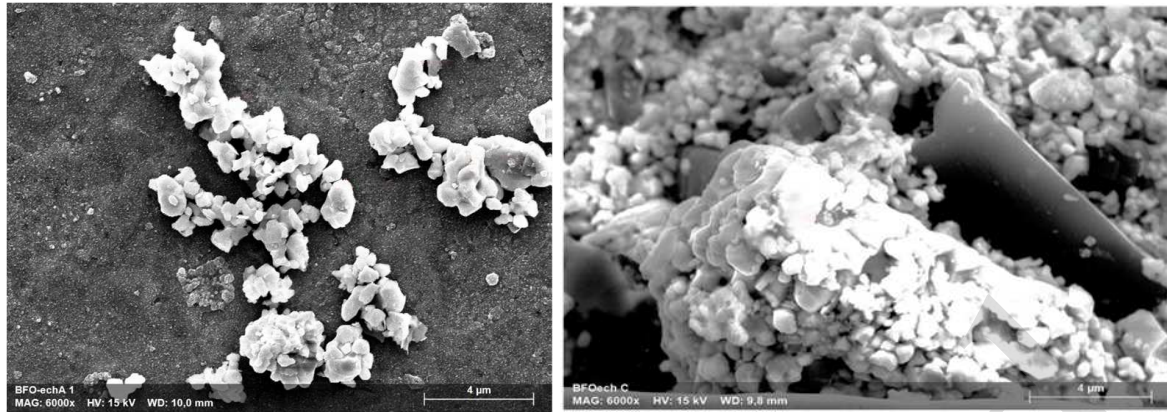


Figure 4. SEM micrographs: a) pure BFO, b) 8% CFs-BFO composites

Table 1. Results of EDX analysis of BFO and CFs-BFO samples

Sample	Number of measurements	Average ion content		
		Bi	Fe	O
BFO	4	0.23	0.24	0.53
4%CFs-BFO	3	0.17	0.23	0.60
8%CFs-BFO	4	0.22	22	0.56
10%CFs-BFO	2	0.21	0.15	0.64

formulation ( $\text{Bi}_{1 \pm \delta}\text{Fe}_{1 \pm \delta}\text{O}_x$ ). In addition, EDX spectra of the  $x\%$ CFs-BFO samples confirmed the presence of carbon fibres.

X-ray diffraction patterns of the BFO and CFs-BFO composite powders, shown in Fig. 5, were analysed by using the X’Pert software. The observed diffraction peaks of the BFO and CFs-BFO samples are in good agreement with the standard  $\text{BiFeO}_3$  diffraction pattern (JCPDS No. 92-210-2910) with the hexagonal phase  $R3c$ , with the strongest  $2\theta$  peaks at  $31.74^\circ$  and  $32.07^\circ$ . They represent the preferential axes of crystal growth oriented along the (104) and (110) planes, respectively. In addition, two weak  $2\theta$  peaks appear at  $27.71^\circ$  and  $32.904^\circ$  corresponding to sillenite ( $\text{Bi}_{25}\text{FeO}_{38.96}$ ) (JCPDS No. 96-901-1269) identified as a secondary phase.

The Rietveld refinement was used for the lattice parameters calculation. The results (not presented here) show that the  $a/c$  ratio is almost constant, indicating that the carbon fibres do not modify the crystal structure of BFO during the hydrothermal treatment.

The average crystallite size,  $D$ , of the BFO particles

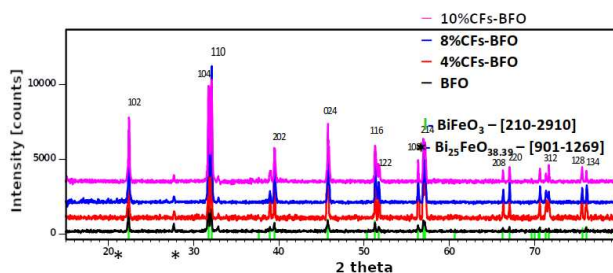


Figure 5. XRD patterns of BFO and CFs-BFO composites

was calculated from Scherrer’s formula:

$$D = \frac{K \cdot \lambda}{\beta \cdot \cos \theta} \quad (2)$$

where  $K$  denotes the Scherrer’s constant ( $K = 0.9$ ),  $\lambda$  is the wavelength of X-ray  $\text{Cu}(K\alpha_1)$  radiation ( $1.5406 \text{ \AA}$ ),  $\beta$  is the full width at half maximum (FWHM) and  $\theta$  is the Bragg’s diffraction angle. The average crystallite size of the BFO particles is about 62 nm and between 73 and 77 nm in the case of the  $x\%$ CFs-BFO composites.

The formation of CFs-BFO composite structure was confirmed by Raman spectroscopy. Figures 6 and 7 show Raman spectra at room temperature of the BFO and  $x\%$ CFs-BFO samples, respectively. The assignments of the vibrational modes were based on a comparison of the obtained Raman results with previous reports for BFO  $R3c$  structure [36–41]. In the BFO sample, 10 active Raman modes were observed. Four peaks at  $138, 170, 220$  and  $469 \text{ cm}^{-1}$  are assigned to  $A_{1-1}, A_{1-2}, A_{1-3}$  and  $A_{1-4}$  vibration modes of the Bi–O band, while the peaks at  $265, 275, 336, 521, 613$  and  $1255 \text{ cm}^{-1}$  are associated with  $E_2, E_3, E_5, E_8, E_9$  and  $2E_9$  vibration modes of the Fe–O band. There is a small difference

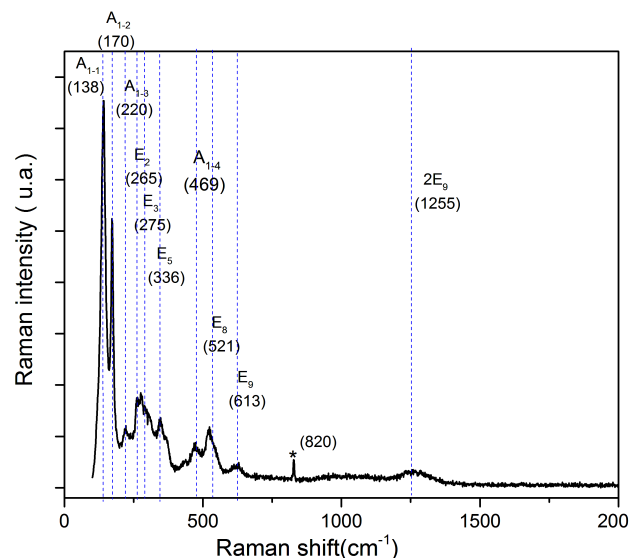


Figure 6. Room-temperature Raman spectrum of BFO

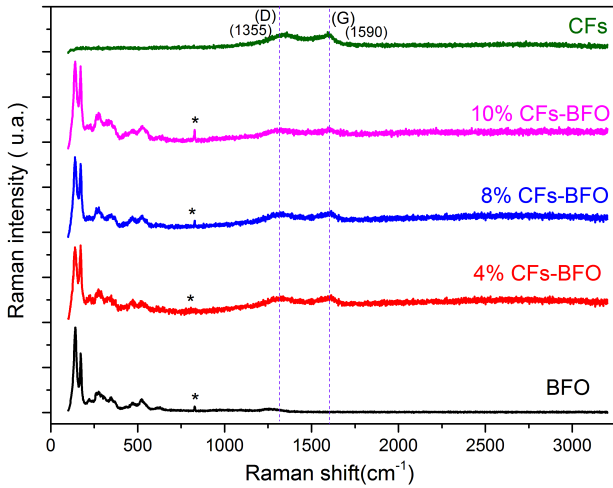


Figure 7. Room-temperature Raman spectra of CFs-BFO composites

in comparison with the literature data, which can be related to the difference in crystallinity or crystallite size. The coexistence of BFO and carbon fibres is confirmed by the Raman spectra of the composites (Fig. 7). Two peaks at 1355 and 1590  $\text{cm}^{-1}$  are attributed to the D-band and G-band of carbon fibres [42,43]. No change is observed on the Raman spectra of BFO phase in the composites, indicating that no phase change occurred during hydrothermal treatment. In addition, the peak at 820  $\text{cm}^{-1}$  observed for all compositions is attributed to the secondary phase (sillenite) which was also detected using X-ray diffraction.

The specific surface area of the BFO and CFs-BFO composite powders was determined from the BET linear plot. BET specific surface area of 3  $\text{m}^2/\text{g}$  was obtained for the pure BFO, whereas much higher values for the composites were obtained, i.e. 104, 205 and 253  $\text{m}^2/\text{g}$  for the 4%CFs-BFO, 8%CFs-BFO and 10%CFs-BFO composite powders, respectively.

### 3.2. Sensing properties

It is well known that the sensitivity of gas sensors is strongly influenced by temperature. In order to determine the optimal operating temperature of the prepared sensitive layers, the sensitivity versus temperature (100–250  $^{\circ}\text{C}$ ) at 100 ppm of acetone was investigated. The gas sensitivity  $S$  (%) is defined by:

$$S = \frac{Z_g - Z_a}{Z_a} \cdot 100 \quad (3)$$

where  $Z_a$  is the electrical impedance of the gas sensor in air and  $Z_g$  is the impedance in the presence of testing gases.

Figure 8 shows a progressive increase in the sensitivity with temperature to reach a maximum value at 200  $^{\circ}\text{C}$  for the BFO sensor, and 180  $^{\circ}\text{C}$  for the  $x\%$ CFs-BFO composite sensors. Above these temperatures, a decrease in sensitivity was observed. So, we deduce that the optimum operating temperatures are 200 and 180  $^{\circ}\text{C}$

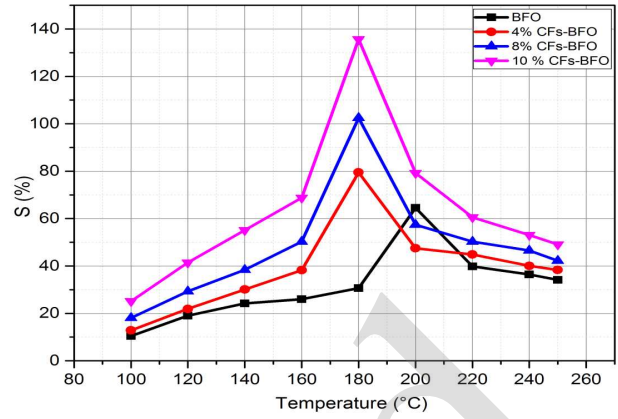


Figure 8. Gas sensing response ( $S$ ) at different operating temperatures of BFO and CFs-BFO composites at 100 ppm of acetone

for the BFO and  $x\%$ CFs-BFO based sensors, respectively.

At temperatures below the optimum operating temperature, low sensitivity values were recorded. This is due to the low adsorption rates of acetone molecules on the sensor surface, which can be attributed to the thermal energy in the chamber which is lower than the energy necessary for the reaction between the acetone molecules and the surface electrons, [16,44]. In contrast, at the optimum operating temperature, the adsorbed acetone molecules have sufficient thermal energy to overcome the activation energy required for their reaction with the oxygen species pre-adsorbed on the BFO surface, which leads to maximal sensitivity. Above this temperature, the desorption rate becomes progressively predominant, leading to a decrease in sensitivity [16,44]. The decrease in the optimum operating temperature of the CFs-BFO composite sensors compared to the BFO sensor may be due to a reduction in activation energy after the addition of carbon fibres. On the other hand, we note an improvement in sensitivity with increasing carbon fibre content in the sensitive layer. This improvement is probably due to the high specific surface area developed by the composites compared to pure BFO, hence the increased number of adsorption sites.

The sensitivity of the BFO and  $x\%$ CFs-BFO sensors as a function of acetone concentration in the range of 50 to 600 ppm is shown in Fig. 9. The results show that the sensitivity of all sensors increases with the increase of the acetone concentration in the environment and can be explained by the increase in the number of surface reactions [45].

The sensitivity of the semiconductor oxide gas sensor can be empirically represented with following two equations [46]:

$$S = \alpha \cdot C^\beta \quad (4)$$

$$\log S = \log \alpha + \beta \log C \quad (5)$$

where  $S$  is the response,  $\alpha$  is the proportionality factor,  $\beta$  is the exponent and  $C$  is the concentration of acetone.

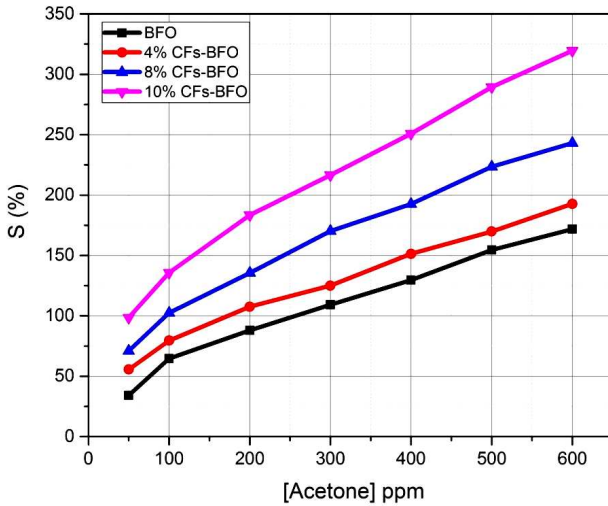


Figure 9. Gas sensing response (*S*) of BFO and CFs-BFO sensors towards various concentrations of acetone

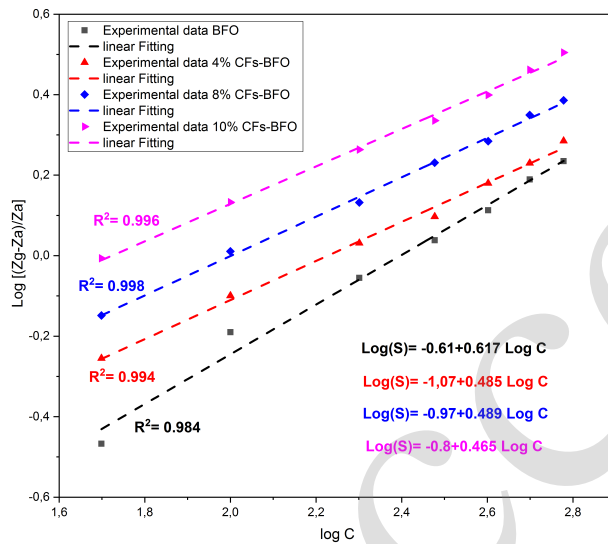


Figure 10. Linear fitting of the sensor's response to different concentrations of acetone

Figure 10 illustrates the variation of  $\log S$  as a function of  $\log C$  for the different sensors. Good linearity is obtained for the different sensors with correlation coefficients  $R^2 = 0.984$  for the pure BFO, and 0.994, 0.998 and 0.996 for 4%CFs-BFO, 8%CFs-BFO and 10%CFs-BFO, respectively. A high degree of linearity indicates that the adsorption of acetone vapour molecules on the surface of our sensors follows a reversible process [47]. The value of the curve slope ( $\beta$ -value) is estimated from the straight-line fit. It is 0.617, 0.485, 0.489 and 0.465 for the BFO, 4%CFs-BFO, 8%CFs-BFO and 10%CFs-BFO sensors, respectively. The  $\beta$  value is nearly 0.5 for all sensors, suggesting that the oxygen adsorbs as  $O^-$  on the sensor's surface [47,48].

Response and recovery times are two essential parameters to evaluate the efficiency of gas sensors. Figure 11 shows the dynamic response-recovery plots of the different sensors. The measurements were realized in an environment containing 100 ppm of acetone. The results

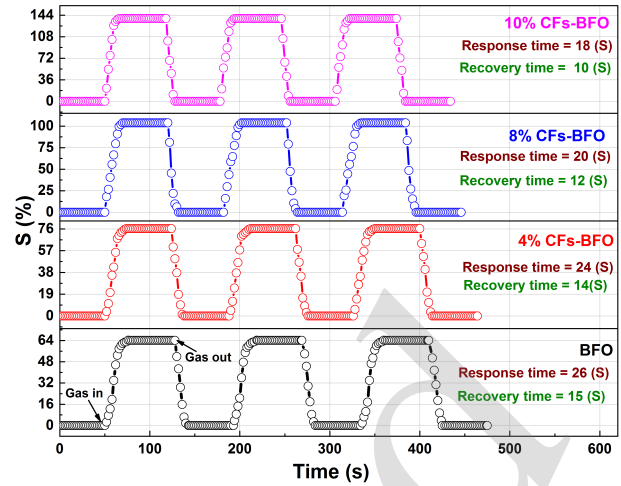


Figure 11. Response and recovery times of BFO and CFs-BFO sensors at 100 ppm of acetone

reveal that all sensors have a perfect combination of excellent sensitivity and reproducibility when exposed to acetone gas. Increasing the carbon fibre content in the compounds significantly decreases the response and recovery times such that the response time decreases from 26 s for the BFO sensor to 18 s for 10%CFs-BFO sensors while the recovery time decreases from 15 to 10 s, respectively.

To confirm the reproducibility of the results, the response and recovery times of two BFO and 10%CFs-BFO based sensors were measured under different acetone gas concentrations (50–300 ppm). As revealed in Fig. 12, excellent reproducibility was obtained.

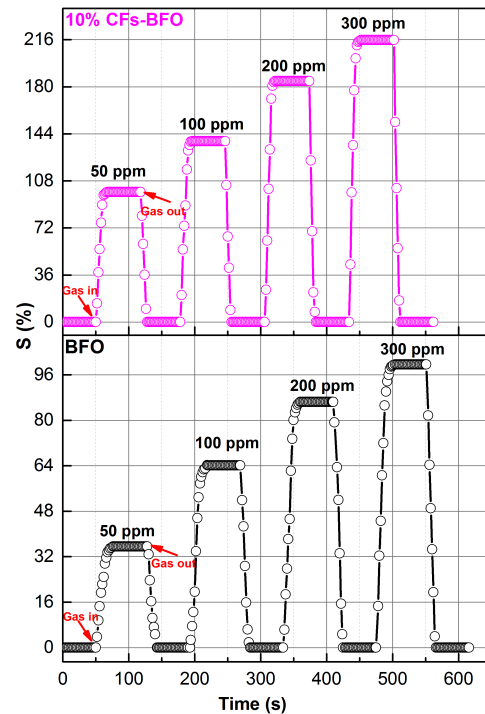
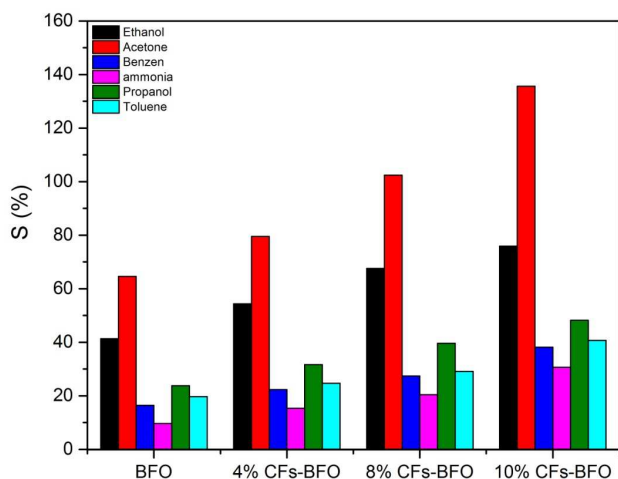
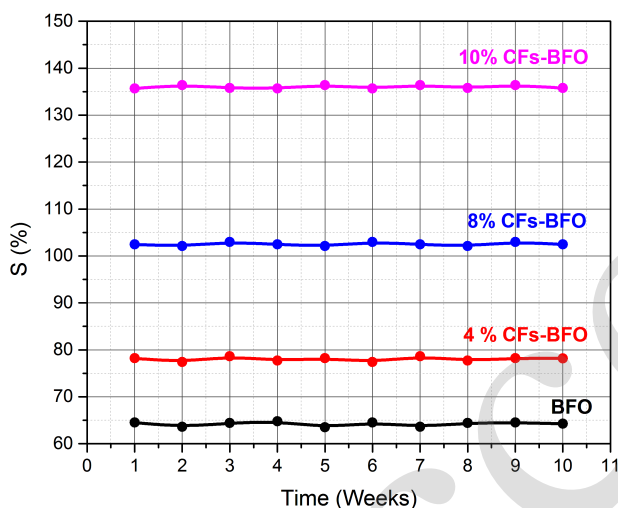


Figure 12. Response and recovery times of BFO and 10% CFs-BFO sensors at different concentrations of acetone



**Figure 13. Gas sensing selectivity of BFO and CFs-BFO sensors to different VOCs at 100 ppm**



**Figure 14. Long-term stability of BFO and CFs-BFO sensors**

The selectivity of all sensors was investigated by testing their sensitivity to six different volatile organic compounds (ethanol, acetone, benzene, ammonia, propanol and toluene). The sensitivity of the sensors to these different gases was measured at a concentration of 100 ppm and the operating temperature of 200 °C for the pure BFO and 180 °C for the  $x\%$ CFs-BFO composite. The results are illustrated in Fig. 13. The results show that the sensors have higher sensitivity for acetone vapour compared to the other volatile organic compounds studied. In addition, the response for each gas was improved by increasing the amount of carbon fibres contained in the composite. The dissociation of VOCs and their interactions with the sensing layer is mainly related to their bond dissociation energy. The selectivity of our sensors for acetone can be attributed to its low bond dissociation energy (352 kJ/mol) compared to that of ethanol (462 kJ/mol), benzene (468 kJ/mol), ammonia (452 kJ/mol), propanol (406 kJ/mol) and toluene (371 kJ/mol), [49,50]. Therefore, acetone gas reacts more easily with the species present at the sensors' surfaces compared to other VOCs studied.

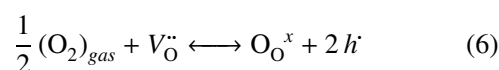
Previous studies have shown that the ferroelectric properties of some semiconductors promote the adsorption of polar molecules, which may interact with the electric polarization of some ferroelectric domains on the surface [51,52]. BiFeO<sub>3</sub> perovskite is known for its strong ferroelectric polarization and exhibits one of the highest spontaneous electrical polarizations  $p = 80 \mu\text{C}/\text{cm}^2$ . This polarity is due to the displacement of the Bi and O sublattices resulting from the stereochemical activity of the 6s lone pair of Bi [53]. Among the volatile organic compounds studied, acetone has the highest dipole moment (2.88 D) followed by ethanol (1.691 D), propanol (1.679 D), ammonia (1.471 D), toluene (0.36 D) and benzene (0 D) [54,55]. Indeed, the high sensitivity of BFO to acetone vapour compared to other VOCs may be attributed to the strong interaction between the dipole moment of the acetone and the spontaneous dipole of the BiFeO<sub>3</sub> perovskite. The results showed that the addition of carbon fibres improved the sensitivity of our sensitive layers. This may be due to the presence of some polar functional groups such as:  $-\text{C}-\text{OH}$ ,  $-\text{C}=\text{O}$  and  $-\text{COOH}$  on the surface of carbon fibres [56].

Long-term stability is also an important factor for gas sensors. It refers to the degradation potential of the sensitive material constituting the sensor. The stability of the prepared sensors was tested for ten weeks under 100 ppm of acetone vapour. Figure 14 shows that all the sensors are very stable and practically no change in their sensitivity was observed during the reported period. This high stability may be due to the preheating of the sensors at 350 °C to achieve thermal stability.

### 3.3. Sensing mechanism

The sensing mechanism of BFO based sensors can be mainly explained by the interaction between the gas molecules and the sensitive layer. When the sensors are exposed to air (without gas), oxygen molecules (O<sub>2</sub>) near the surface attract electrons from the valence band of BFO and adsorb at the sensor surface as O<sup>-</sup>, O<sup>2-</sup> or O<sub>2</sub><sup>-</sup>. As our sensors operate at temperatures of 200 °C (the pure BFO) and 180 °C (the CFs-BFO), the O<sup>-</sup> species are more dominant than other adsorbed oxygen species [57].

The p-type semiconducting character of BFO, the adsorption process of oxygen species and the reaction between atmospheric oxygen and oxygen vacancies in the perovskite structure increase the accumulation of positive charges (holes) on the surface (Eq. 6). Hence, the increase of the electrical conductivity of the sensitive films reduces their electrical impedance [14].



Equations 7-9 describe the detection mechanism for acetone gas [51,58]. The acetone molecules adsorb and interact with the O<sup>-</sup> pre-adsorbed on the surface of the sensor with the reinjection of electrons in the valence



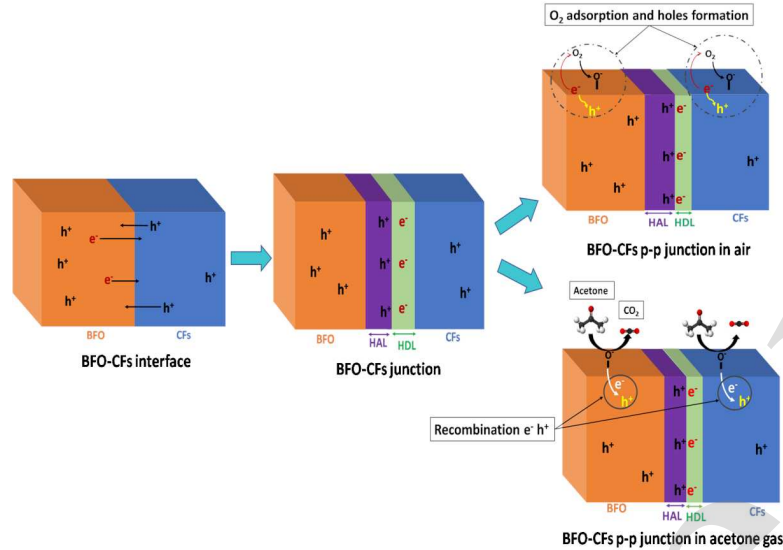
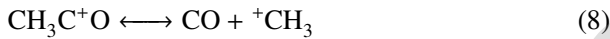
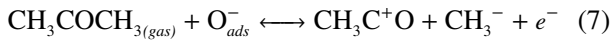


Figure 15. Schematic diagrams of gas sensing mechanism of CFs-BFO p-p junction

band of the semiconductor. These electrons recombine with the holes and lead to an increase in the impedance of the sensitive films [16].



In the case of the CFs-BFO composite, the formation of a p-p junction at the interface between BFO and CFs can be a real factor in improving gas sensing performance. Due to their different work function (WF), electrons are transferred from the BFO material with low WF ( $\varphi_{\text{BFO}} = 4.5 \text{ eV}$ ) [59] to the CFs material with high WF ( $\varphi_{\text{CFs}} = 4.7 \text{ eV}$ ) [60]. Thus, it reaches a stable state and forms a new Fermi energy level. A hole depletion layer (HDL) gradually forms at the CFs interface and a hole accumulation layer (HAL) forms at the BFO interface [61]. It has also been reported that the resistance of p-p junctions depends on the thickness of the HAL [62]. In the air, oxygen molecules capture elec-

trons from CFs and the formed holes are transferred to the valence band of CFs and then to the HDL. During this process, the HDL will be less depleted. At the same time on the BFO side, more electrons are trapped by the adsorbed oxygen, leaving more holes near the BFO surface. Once the composite has been exposed to the acetone vapour, the  $\text{O}^-$  pre-adsorbed on the surface reacts with the acetone molecule to release electrons, which recombine with the holes previously formed. This process reduces the thickness of the HAL, which leads to an increase in impedance [62]. Figure 15 displays a scheme of the adsorption mechanism at the CFs-BFO interface.

For a better evaluation of the gas sensing performance of the prepared sensors, a comparison between the present study and similar works carried out previously [63–70] is summarized in Table 2. This comparison confirms that the BFO-based sensor exhibits comparable acetone sensing characteristics in terms of selectivity, operating temperature and response/recovery times. These results show that the CFs-BFO composite based materials are promising materials for gas sensor applications.

Table 2. Comparison of acetone sensing properties (response, response time  $\tau_{\text{res}}$ , and recovery time  $\tau_{\text{rec}}$ ) of BFO, CFs-BFO and various metal oxide nanostructure-based sensors

Sensing material	Operating temperature [°C]	Concentration [ppm]	Response [%]	$\tau_{\text{res}}/\tau_{\text{rec}}$ [s]	Ref.
CuO (thin film)	250	300	133 <sup>(a)</sup>	27 / 248	[63]
rGO/In <sub>2</sub> O <sub>3</sub>	175	25	85 <sup>(a)</sup>	- / -	[64]
La <sub>0.9</sub> Sr <sub>0.1</sub> CoO <sub>3</sub>	25	50	21 <sup>(a)</sup>	20 / 25	[65]
Au-CNT	25	800	4.6 <sup>(a)</sup>	- / -	[66]
3D-printed CuO/Cu <sub>2</sub> O/Cu	350	100	150 <sup>(a)</sup>	- / -	[67]
Ag/MWCNTs	25	800	3.43 <sup>(a)</sup>	- / -	[68]
rGO-RB composite	25	1000	1.01 <sup>(a)</sup>	- / -	[69]
MXene/rGO/CuO	25	100	52 <sup>(a)</sup>	6.5 / 7.5	[70]
BiFeO <sub>3</sub> particles	200	100	64 <sup>(b)</sup>	26 / 15	This work
10% CFs-BiFeO <sub>3</sub> composite	180	100	135 <sup>(b)</sup>	18 / 10	This work

<sup>(a)</sup> Response was defined as  $(R_g - R_a)/R_a \times 100$

<sup>(b)</sup> Response was defined as  $(Z_g - Z_a)/Z_a \times 100$

#### IV. Conclusions

Pure BiFeO<sub>3</sub> (BFO) particles were synthesized by sol-gel method and used for obtaining composites with carbon fibres (*x*%CFs-BFO, where *x* corresponds to 4, 8 and 10 wt.%) by hydrothermal treatment at 150 °C. XRD, SEM-EDX and Raman characterizations confirmed the formation of BFO phase in all samples and presence of CFs in the composites. BET specific surface areas of the prepared BFO, 4%CFs-BFO, 8%CFs-BFO and 10%CFs-BFO powders were 3, 104, 205 and 253 m<sup>2</sup>/g, respectively.

The results of adsorption tests of various VOCs on the surface of the pure BFO and *x*%CFs-BFO composite-based sensors showed that the adsorption process is reversible. In addition, high selectivity to acetone vapour was noted. The sensors developed from the synthesized 10%CFs-BFO composite show very good sensitivity of up to 135% at 100 ppm of acetone vapour, which is two times higher than that of the pure BFO. Moreover, the addition of carbon fibres reduced significantly the response/recovery time and optimum operating temperature from 200 to 180 °C.

The combination of increased surface area and electrical conductivity due to the addition of carbon fibres plays a crucial role in improving the detection properties. The observed sensing properties of the CFs-BFO composites are very promising, which makes these materials excellent candidates for the development of gas sensors with high detection potential.

#### References

1. A. Mirzaei, S.G. Leonardi, G. Neri, "Detection of hazardous volatile organic compounds (VOCs) by metal oxide nanostructures based gas sensors: A review", *Ceram. Int.*, **42** [14] (2016) 15119–15141.
2. P. Patnaik, *A Comprehensive Guide to the Hazardous Properties of Chemical Substances*, John Wiley & Sons, New Jersey, 2007.
3. X. Zhang, B. Gao, A.E. Creamer, C. Cao, Y. Li, "Adsorption of VOCs onto engineered carbon materials: A review", *J. Hazard. Mater.*, **338** (2017) 102–123.
4. J.H.E. Arts, J. Mojet, L.J.V. Gemert, H.H. Emmen, J.H.C.M. Lammers, J. Marquart, R.A. Woutersen, V.J. Feron, "An analysis of human response to the irritancy of acetone vapors", *Crit. Rev. Toxicol.*, **32** (2002) 43–66.
5. Q. Jia, H. Ji, Y. Zhang, Y. Chen, X. Sun, Z. Jin, "Rapid and selective detection of acetone using hierarchical ZnO gas sensor for hazardous odor markers application", *J. Hazard. Mater.*, **276** (2014) 262–270.
6. J.S. Do, S.H. Wang, "On the sensitivity of conductimetric acetone gas sensor based on polypyrrole and polyaniline conducting polymers", *Sens. Actuat. B*, **185** (2013) 39–46.
7. C. Wang, L.i Yin, L. Zhang, D. Xiang, R. Gao, "Metal oxide gas sensors: Sensitivity and influencing factors", *Sensors*, **10** [3] (2010) 2088–2106.
8. A. Dey, "Semiconductor metal oxide gas sensors: A review", *Mater. Sci. Eng. B*, **229** (2018) 206–217.
9. X.L. Yu, Y. Wang, Y.M. Hu, C.B. Cao, H.L.W. Chan, "Gas-sensing properties of perovskite BiFeO<sub>3</sub> nanoparticles", *J. Am. Ceram. Soc.*, **92** [12] (2009) 3105–3107.
10. N. Wang, X. Luo, L. Han, Z. Zhang, R. Zhang, H. Olin, Y. Yang, "Structure, performance, and application of BiFeO<sub>3</sub> nanomaterials", *Nano-Micro Lett.*, **12** (2020) 81.
11. S.D. Waghmare, V.V. Jadhav, S.K. Gore, S.J. Yoon, S.B. Ambade, B.J. Lokhande, R.S. Mane, S.H. Han, "Efficient gas sensitivity in mixed bismuth ferrite micro (cubes) and nano (plates) structures", *Mater. Res. Bull.*, **47** [12] (2012) 4169–4173.
12. M. Dziubaniuk, R. Bujakiewicz-Koronska, J. Suchanicz, J. Wyrwa, M. Rekas, "Application of bismuth ferrite protonic conductor for ammonia gas detection", *Sens. Actuat. B*, **188** (2013) 957–964.
13. S. Das, S. Rana, S.K.M. Mursalin, P. Rana, A. Sen, "Sonochemically prepared nanosized BiFeO<sub>3</sub> as novel SO<sub>2</sub> sensor", *Sens. Actuat. B*, **218** (2015) 122–127.
14. G. Dong, H. Fan, H. Tian, J. Fang, Q. Li, "Gas-sensing and electrical properties of perovskite structure p-type barium-substituted bismuth ferrite", *RSC Adv.*, **5** [38] (2015) 29618–29623.
15. T. Tong, J. Chen, D. Jin, J. Cheng, "Preparation and gas sensing characteristics of BiFeO<sub>3</sub> crystallites", *Mater. Lett.*, **197** (2017) 160–162.
16. Y. Zhang, H. Xu, S. Dong, R. Han, X. Liu, Y. Wang, S. Li, Q. Bu, X. Li, J. Xiang, "A fast response and recovery acetone gas sensor based on BiFeO<sub>3</sub> nanomaterials with high sensitivity and low detection limit", *J. Mater. Sci. Mater. Electron.*, **29** [3] (2017) 2193–2200.
17. S. Chakraborty, M. Pal, "Highly selective and stable acetone sensor based on chemically prepared bismuth ferrite nanoparticles", *J. Alloys Compd.*, **787** (2019) 1204–1211.
18. R. Douani, N. Lamrani, M. Oughanem, M. Saidi, Y. Guhel, A. Chaouchi, B. Boudart, "Improvement of humidity sensing performance of BiFeO<sub>3</sub> nanoparticles-based sensor by the addition of carbon fibers", *Sens. Actuat. A*, **307** (2020) 111981.
19. J. An, L. Zhu, Y. Zhang, H. Tang, "Efficient visible light photo-Fenton-like degradation of organic pollutants using in situ surface-modified BiFeO<sub>3</sub> as a catalyst", *J. Environ. Sci.*, **25** [6] (2013) 1213–1225.
20. T. Tong, H. Zhang, J. Chen, D. Jin, J. Cheng, "The photocatalysis of BiFeO<sub>3</sub> disks under visible light irradiation", *Catal. Commun.*, **87** (2016) 23–26.
21. C. Tablero, "An evaluation of BiFeO<sub>3</sub> as a photovoltaic material", *Sol. Energy Mater. Sol. Cells.*, **171** (2017) 161–165.
22. O. Ceballos-Sanchez, A. Sanchez-Martinez, F.J. Flores-Ruiz, A.M. Huerta-Flores, L.M. Torres-Martinez, R. Ruelas, M. Garcia-Guaderrama, "Study of BiFeO<sub>3</sub> thin film obtained by a simple chemical method for the heterojunction-type solar cell design", *J. Alloys Compd.*, **832** (2020) 154923.
23. K. Shirvanimoghaddam, S.U. Hamim, M.K. Akbari, S.M. Fakhroshini, H. Khayyam, A.H. Pakseresht, E. Ghasali, M. Zabet, K.S. Munir, S. Jia, J.P. Davim, M. Naebe, "Carbon fiber reinforced metal matrix composites: Fabrication processes and properties", *Composites: Part A*, **92** (2017) 70–96.
24. N. Gupta, S.M. Gupta, S.K. Sharma, "Carbon nanotubes: Synthesis, properties and engineering applications", *Carbon Lett.*, **29** (2019) 419–447.
25. Y. Zhu, S. Murali, W. Cai, X. Li, J. W. Suk, J.R. Potts, R.S. Ruoff, "Graphene and graphene oxide: Synthesis, proper-

- ties, and applications”, *Adv. Mater.*, **22** (2010) 3906–3924.
26. A. Goldoni, V. Alijani, L. Sangaletti, L. D’Arsiè, “Advanced promising routes of carbon/metal oxides hybrids in sensors: A review”, *Electrochim. Acta.*, **266** (2018) 139–150.
  27. Z. Wenrui, M. Fanxing, Q. Yanan, C. Fei, Y. Haitao, Z. Minwei, “Fabrication and specific functionalisation of carbon fibers for advanced flexible biosensors”, *Front. Chem.*, **8** (2020) 855–867.
  28. W. Tian, X. Liu, W. Yu, “Research progress of gas sensor based on graphene and its derivatives: A review”, *Appl. Sci.*, **8** (2018) 1118–1139.
  29. J. Kaur, K. Anand, A. Kaur, R.C. Singh, “Sensitive and selective acetone sensor based on Gd doped WO<sub>3</sub>/reduced graphene oxide nanocomposite”, *Sens. Actuat. B*, **258** (2018) 1022–1035.
  30. F. Mendoza, D.M. Hernández, V. Makarova, E. Febus, B.R. Weiner, G. Morell, “Room temperature gas sensor based on tin dioxide-carbon nanotubes composite films”, *Sens. Actuat. B*, **190** (2014) 227–233.
  31. B. Zhang, J. Liu, X. Cui, Y. Wang, Y. Gao, P. Sun, F. Liu, K. Shimanoe, N. Yamazoe, G. Lu, “Enhanced gas sensing properties to acetone vapor achieved by  $\alpha$ -Fe<sub>2</sub>O<sub>3</sub> particles ameliorated with reduced graphene oxide sheets”, *Sens. Actuat. B*, **241** (2017) 904–914.
  32. B. Zhang, G. Liu, M. Cheng, Y. Gao, L. Zhao, S. Li, F. Liu, X. Yan, T. Zhang, P. Sun, G. Lu, “The preparation of reduced graphene oxide-encapsulated  $\alpha$ -Fe<sub>2</sub>O<sub>3</sub> hybrid and its outstanding NO<sub>2</sub> gas sensing properties at room temperature”, *Sens. Actuat. B*, **261** (2018) 252–263.
  33. T. Hojati, M. Ebrahimi, R. Afzalzadeh, “Highly sensitive CO sensor based on ZnO/MWCNT nano sheet network grown via hydrothermal method”, *Mater. Chem. Phys.*, **207** (2018) 50–57.
  34. P. Sun, C. Wang, X. Zhou, P. Cheng, K. Shimanoe, G. Lu, N. Yamazoe, “Cu-doped  $\alpha$ -Fe<sub>2</sub>O<sub>3</sub> hierarchical microcubes: Synthesis and gas sensing properties”, *Sens. Actuat. B*, **193** (2014) 616–622.
  35. J.H. Xu, H. Ke, D.C. Jia, W. Wang, Y. Zhou, “Low-temperature synthesis of BiFeO<sub>3</sub> nanopowders via a sol-gel method”, *J. Alloys Compd.*, **472** [1–2] (2009) 473–477.
  36. A. Amouri, S. Aydi, N. Abdelmoula, H. Dammak, H. Khemakhem, “Evidence of magnetoelectric coupling in 0.9BiFeO<sub>3</sub>-0.1Ba[Ti<sub>0.95</sub>(Yb<sub>0.5</sub>Nb<sub>0.5</sub>)<sub>0.05</sub>]O<sub>3</sub> ceramic”, *J. Alloys Compd.*, **739** (2018) 1065–1079.
  37. Y. Yang, J.Y. Sun, K. Zhu, Y.L. Liu, L., “Structure properties of BiFeO<sub>3</sub> films studied by micro-Raman scattering”, *J. Appl. Phys.*, **103** (2008) 093532–093536.
  38. Y.H. Si, Y. Xia, S.K. Shang, X.B. Xiong, X.R. Zeng, J. Zhou, Y.Y. Li, “Enhanced visible light driven photocatalytic behavior of BiFeO<sub>3</sub>/reduced graphene oxide composites”, *Nanomaterials*, **8** (2018) 526–538.
  39. J.L. Ortiz-Quinonez, U. Pal, M.S. Villanueva, “Effects of oxidizing/reducing agent ratio on phase purity, crystallinity, and magnetic behavior of solution-combustion-grown BiFeO<sub>3</sub> submicroparticles”, *Inorg. Chem.*, **57** [10] (2018) 6152–6160.
  40. T. Wang, S.H. Song, X.L. Wang, J.J. Chen, M.L. Tan, “Chemical substitution-induced structure transition and enhanced magnetic and optical properties of sol-gel synthesized multiferroic BiFeO<sub>3</sub> nanoparticles”, *J. Sol-Gel Sci. Technol.*, **85** [2] (2017) 356–368.
  41. A. Kumar, P. Sharma, W. Yang, J. Shen, D. Varshney, Q. Li, “Effect of La and Ni substitution on structure, dielectric and ferroelectric properties of BiFeO<sub>3</sub> ceramics. Ceramics International”, *Ceram. Int.*, **42** [13] (2016) 14805–14812.
  42. X. Liu, H. Dong, Y. Li, “Characterization of thermal conductivity of carbon fibers at temperatures as low as 10 K”, *Int. J. Thermophys.*, **39** [8] (2018) 97.
  43. P. Musiol, P. Szatkowski, M. Gubernat, A. Weselucha-Birczynska, S. Blazewicz, “Comparative study of the structure and micro structure of PAN-based nano- and micro-carbon fibers”, *Ceram. Int.*, **42** [10] (2016) 11603–11610.
  44. X. Li, D. Li, J. Xu, H. Jin, D. Jin, X. Peng, B. Hong, J. Li, Y. Yang, H. Ge, X. Wang, “Calcination-temperature-dependent gas-sensing properties of mesoporous nickel oxides nanowires as ethanol sensors”, *Powder Technol.*, **318** (2017) 40–45.
  45. A. Sutka, G. Mezinskis, A. Lasis, D. Jakovlevs, “Influence of iron non-stoichiometry on spinel zinc ferrite gas sensing properties”, *Sens. Actuat. B*, **171** (2012) 204–209.
  46. M. Sinha, R. Mahapatra, B. Mondal, T. Maruyama, R. Ghosh, “Ultra-fast and reversible gas sensing properties of ZnO nanowire arrays grown by hydrothermal technique”, *J. Phys. Chem. C*, **120** [5] (2016) 3019–3025.
  47. S. Neogi, R. Ghosh, “Origin of irreversible to reversible transition in acetone detection for Y-doped BiFeO<sub>3</sub> perovskite”, *J. Appl. Phys.*, **128** [14] (2020) 144501–144513.
  48. S. Chakraborty, M. Pal, “Improved sensitivity of CdS nanoparticles by virtue of calcium doping: Promising candidate for monitoring alcohol in exhale human breath”, *Mater. Des.*, **126C** (2017) 18–28.
  49. J. Li, P. Tang, J. Zhang, Y. Feng, R. Luo, A. Chen, D. Li, “Facile synthesis and acetone sensing performance of hierarchical SnO<sub>2</sub> hollow microspheres with controllable size and shell thickness”, *Ind. Eng. Chem. Res.*, **55** [12] (2016) 3588–3595.
  50. J.W. Jeon, D.H. Lee, Y.S. Won, M.G. Lee, “Characteristics of photocatalytic decomposition of individual and binary mixture vapors of some VOCs by a cylindrical UV reactor with helically installed TiO<sub>2</sub>-coated perforated planes”, *Korean J. Chem. Eng.*, **35** (2018) 744–749.
  51. Y. Yun, L. Kampschulte, M. Li, D. Liao, E.I. Altman, “Effect of ferroelectric poling on the adsorption of 2-propanol on LiNbO<sub>3</sub> (0001)”, *J. Phys. Chem. C*, **111** [37] (2007) 13951–13956.
  52. S. Liu, F. Zhang, H. Li, T. Chen, Y. Wang, “Acetone detection properties of single crystalline tungsten oxide plates synthesized by hydrothermal method using cetyltrimethyl ammonium bromide supermolecular template”, *Sens. Actuat. B*, **162** [1] (2012) 259–268.
  53. J.G. Park, M.D. Le, J. Jeong, S. Lee, “Structure and spin dynamics of multiferroic BiFeO<sub>3</sub>”, *J. Phys. Condens. Matter.*, **26** [34] (2014) 433202–433235.
  54. C.L. Yaws, P.K. Narasimhan, “Dipole moment - Organic compounds”, pp. 672–682 in *Thermophysical Properties of Chemicals and Hydrocarbons*, Ed. L.Y. Carl, William Andrew Publishing, Norwich, NY, 2009.
  55. L. Wang, K. Kalyanasundaram, M. Stanacevic, P. Gouma, “Nanosensor device for breath acetone detection”, *Sens. Lett.*, **8** [5] (2010) 709–712.
  56. J.J. Sha, J.X. Dai, J. Li, Z. Q. Wei, J.M. Hausherr, W. Krenkel, “Influence of thermal treatment on thermo-mechanical stability and surface composition of carbon fiber”, *Appl. Surf. Sci.*, **274** (2013) 89–94.

57. J.M. Walker, S.A. Akbar, P.A. Morris, “Synergistic effects in gas sensing semiconducting oxide nano-heterostructures: A review”, *Sens. Actuat. B*, **286** (2019) 624–640.
58. X. Yu, F. Song, B. Zhai, C. Zheng, Y. Wang, “Electrospun ZnO nanotubes and its gas sensing applications”, *Physica E*, **52** (2013) 92–96.
59. T. Shi, J. Wang, W. Yan, X. Shao, Z.L. Hou, “Enhanced photovoltaic property based on reduced leakage current and band gap in Nd-doped BiFeO<sub>3</sub> films”, *Mater. Res. Express*, **6** (2019) 086426.
60. A.F. Bobkov, E.V. Davydov, S.V. Zaitsev, A.V. Karpov, M.A. Kozodaev, I.N. Nikolaeva, M.O. Popov, E.N. Skorokhodov, A.L. Suvorov, Yu.N. Cheblukov, “The use of carbonaceous materials as field-emission cathodes”, *Tech. Phys.*, **46** [6] (2001) 736–742.
61. P. Hao, G. Qiu, P. Song, Z. Yang, Q. Wang, “Construction of porous LaFeO<sub>3</sub> microspheres decorated with NiO nanosheets for high response ethanol gas sensors”, *Appl. Surf. Sci.*, **515** (2020) 146025.
62. S. Bai, L. Du, J. Sun, R. Luo, D. Li, A. Chen, C.C. Liub, “Preparation of reduced graphene oxide/Co<sub>3</sub>O<sub>4</sub> composites and sensing performance to toluene at low temperature”, *RSC Adv.*, **6** (2016) 60109–60116.
63. A. Ghosh, A. Maity, R. Banerjee, S.B. Majumder, “Volatile organic compound sensing using copper oxide thin films: Addressing the cross sensitivity issue”, *J. Alloys Compd.*, **692** (2017) 108–118.
64. R.K. Mishra, G. Murali, T. Kim, J.H. Kim, Y.J. Lim, B.S. Kim, P.P. Sahayd, S.H. Lee, “Nanocube In<sub>2</sub>O<sub>3</sub>@RGO heterostructure based gas sensor for acetone and formaldehyde detection”, *RSC Adv.*, **7** (2017) 38714–38724.
65. H. Liu, Y. Guo, R. Xie, T. Peng, G. Ma, Y. Tang, “Novel acetone sensing performance of La<sub>1-x</sub>Sr<sub>x</sub>CoO<sub>3</sub> nanoparticles at room temperature”, *Sens. Actuat. B*, **246** (2017) 164–168.
66. S.J. Young, Z.D. Lin, “Acetone gas sensors composed of carbon nanotubes with adsorbed Au nanoparticles on plastic substrate”, *Microsyst Technol.*, **24** (2018) 3973–3976.
67. L. Siebert, O. Lupan, M. Mirabelli, N. Ababii, M. Terasa, S. Kaps, V. Cretu, A. Vahl, F. Faupel, R. Adelung, “3D-printed chemiresistive sensor array on nanowire CuO/Cu<sub>2</sub>O/Cu heterojunction nets”, *ACS Appl. Mater. Interfaces*, **11** (2019) 25508–25515.
68. S. Young, Y. Liu, Z. Lin, K. Ahmed, M.N.I. Shiblee, S. Romanuik, P.K. Sekhar, T. Thundat, L. Nagahara, S. Arya, R. Ahmed, H. Furukawa, A. Khosla, “Multi-walled carbon nanotubes decorated with silver nanoparticles for acetone gas sensing at room temperature”, *J. Electrochem. Soc.*, **167** (2020) 167519.
69. R. Kumar, R. Ghosh, “Selective determination of ammonia, ethanol and acetone by reduced graphene oxide based gas sensors at room temperature”, *Sen. Bio-Sen. Res.*, **28** (2020) 100336.
70. M. Liu, Z. Wang, P. Song, Z. Yang, Q. Wang, “Flexible MXene/rGO/CuO hybrid aerogels for high performance acetone sensing at room temperature”, *Sens. Actuat. B*, **340** (2021) 129946.